2017

A 3D hierarchical porous Co3O4 nanotube network as an efficient cathode for rechargeable lithium-oxygen batteries

Lili Liu
University of Wollongong, Nanjing Tech University, ll422@uowmail.edu.au

Haipeng Guo
University of Wollongong, hg476@uowmail.edu.au

Yuyang Hou
University of Wollongong, yh879@uowmail.edu.au

Jun Wang
Shandong University, jw707@uowmail.edu.au

Lijun Fu
Nanjing Tech University

See next page for additional authors

Publication Details

Liu, L., Guo, H., Hou, Y., Wang, J., Fu, L., Chen, J., Liu, H., Wang, J. & Wu, Y. (2017). A 3D hierarchical porous Co3O4 nanotube network as an efficient cathode for rechargeable lithium-oxygen batteries. Journal of Materials Chemistry A, 5 (28), 14673-14681.

A 3D hierarchical porous Co3O4 nanotube network as an efficient cathode for rechargeable lithium-oxygen batteries

Abstract

Herein, a three-dimensional (3D) hierarchical porous Co 3 O 4 nanotube (Co 3 O 4 HPNT) network was prepared using a polypyrrole nanofiber (PPyNF) as a sacrificial template. When employed as a cathode for lithium-oxygen batteries, the 3D Co 3 O 4 HPNT network demonstrated superior bifunctional electrocatalytic activities towards both the oxygen reduction reaction (ORR) and the oxygen evolution reaction (OER), with a relatively low charge overpotential of 99 mV and a high discharge/charge capacity of 4164/4299 mA h g -1 . High-resolution scanning electron microscopy, X-ray diffraction, and X-ray photoelectron spectroscopy measurements on Co 3 O 4 HPNT-based cathode after discharge/recharge showed reversible formation and decomposition of Li 2 O 2 . This superior performance is ascribed to the 3D web-like porous tubular structure, which facilitates rapid oxygen flow, provides enough void volume for insoluble Li 2 O 2 deposition, and increases the catalytic utilization of Co 3 O 4 . Moreover, the hierarchical porous structure with meso-/nanopores on the walls of the Co 3 O 4 nanotubes facilitates O 2 diffusion, electrolyte penetration, and mass transport of all the reactants.

Disciplines

Engineering | Physical Sciences and Mathematics

Publication Details

Liu, L., Guo, H., Hou, Y., Wang, J., Fu, L., Chen, J., Liu, H., Wang, J. & Wu, Y. (2017). A 3D hierarchical porous Co3O4 nanotube network as an efficient cathode for rechargeable lithium-oxygen batteries. Journal of Materials Chemistry A, 5 (28), 14673-14681.

Authors

Lili Liu, Haipeng Guo, Yuyang Hou, Jun Wang, Lijun Fu, Jun Chen, Hua-Kun Liu, Jiazhao Wang, and Yu-Ping Wu

3D Hierarchical Porous Co_3O_4 Nanotube Network as Efficient Cathode for Rechargeable Lithium-Oxygen Batteries

Lili Liu, Haipeng Guo, Yuyang Hou, Jun Wang, Jun Chen, Hua-Kun Liu, Jiazhao Wang and Yuping Wu**

[*]L. Liu, Dr. Prof. Y. Wu
College of Energy and Institute for Advanced Materials, Nanjing Tech University
Jiangsu Province, Nanjing 211816, China
E-mail: wuyp@fudan.edu.cn

[*]L. Liu, H. Guo, Dr. Prof. H. Liu, Dr. Prof. J. Wang
Institute for Superconducting and Electronic Materials, University of Wollongong, Wollongong, New South Wales 2522, Australia
E-mail: jiazhao@uow.edu.au

Y. Hou, Dr. J. Chen
Intelligent Polymer Research Institute, University of Wollongong, Wollongong, New South Wales 2522, Australia

Dr. J. Wang
Key Laboratory for Liquid-Solid Structural Evolution and Processing of Materials, Ministry of Education, Shandong University, Jinan 250061, PR China;
Engineering Ceramics Key Laboratory of Shandong Province, Shandong University, 250061, PR China

Dr. Prof. Y. Wu
Department of Chemistry, Fudan University, Shanghai 200433, China

Keywords: 3D porous nanotube, Co_3O_4, ORR, OER, lithium-oxygen batteries

Abstract

An approach to synthesize three-dimensional (3D) hierarchical porous Co_3O_4 nanotube (Co_3O_4 HPNT) network has been proposed. Polypyrrole nanofiber (PPyNF) is used as the sacrificial template. The present technique may offer a new strategy for the design and synthesis of 3D structured porous nanotubular materials. When employed as cathode for lithium oxygen batteries, the 3D Co_3O_4 HPNT network demonstrated superior bi-functional electrocatalytic activities towards both the oxygen reduction reaction (ORR) and the oxygen evolution reaction (OER), with a rather low charge overpotential of 99 mV and high

discharge/charge capacity of 4164/4299 mAh g^{-1}. High resolution scanning electron microscope, X-ray diffraction, and X-ray photoelectron spectroscopy measurements on Co_3O_4 HPNT based cathode after discharge/recharge showed reversible Li_2O_2 formation and decomposition. This promising performance is ascribed to the 3D web-like porous tubular structure, which facilitates rapid oxygen flow, provides enough void volume for insoluble Li_2O_2 deposition, and increases the catalytic utilization of Co_3O_4. Meanwhile, the hierarchical porous structure with meso/nanopores on the walls of the Co_3O_4 nanotubes facilitates O_2 diffusion, electrolyte penetration, and mass transport of all the reactants.

1. Introduction

Nanotechnology has definitely promoted the progress of material science and inspired the global chemists to think and act via a nano-perspective[1, 2]. Increasingly significant achievements have been obtained in the research field of energy storage systems, electrocatalysis and fuel cells based on the concept of nanostructured materials[3-9]. 3D hierarchical porous nanotube (HPNT) material will show further superiorities compared with the currently developed nanotechnology. Firstly, the continuous 3D conductive network can greatly improve the charge transport (in the electrolyte and the active materials) and charge transfer (in the two-phase interface), facilitating the electrode reaction kinetics and reaction rate[2, 10-13]. Secondly, the nanoporous tubular structure with enlarged surface area can facilitate rapid ion and electron transport, improve adsorption of and immersion in electrolyte on the surfaces of electroactive materials, and enhance the capacity and energy density[6, 14-16]. More importantly, the HPNT structured materials will beneficial to the development of promising lithium oxygen battery which require optimal cathode structure to afford repaid oxygen reduction reaction (ORR) and oxygen evolution reaction (OER) kinetics[17-21]. The macroscale spaces in the 3D network skeleton can function as “highways” to continuously supply oxygen to the interior parts of the electrode [22-24]. 3D nanoporous tubes are instinctively connected to a

whole network, which greatly reduce the interface contact impedance compared to the reported 1D nanoporous tubes[25]. Moreover, the larger porosity on the nanotube can create more abundant tri-phase (catalyst-electrolyte-oxygen) regions required by ORR and OER[23, 24], because O_2 and electrolyte can enter into the hollow cavities of porous nanotubes via not only the two narrow ends but also holes along the tube wall. In addition, the macropores and nanoporoes provide sufficient space for discharge product (Li_2O_2) deposition, which enlarges the discharge capacity[6, 26]. To the best of our knowledge however, there has not been reported yet on the synthesis of the 3D HPNT network structure for Li-O_2 battery application.

In the previous reports, fabrication 1D porous nanotubes mere has been evidenced a critical challenge, since it involves either a multistep synthetic route[23, 27] or precious metal as template[28, 29]. We present here a facile and scalable fabrication scheme for a 3D hierarchical porous Co_3O_4 nanotube (Co_3O_4 HPNT) network by employing polypyrrole (PPy) nanofiber as a sacrificial template. The PPy nanofiber template with its unique 3D nanoweb morphology is cheaper, easier to be synthesized by a facile chemical polymerization method in a large scale compared with other templates e.g. Al_2O_3 array that needs complicated electrochemical deposition[30, 31]. Its easy and thorough removal by a direct heat treatment in air atmosphere makes it undoubtedly a much superior approach to the fabrication of tubular structures compared with other inorganic templates to produce porosity[32, 33]. Take SiO_2 template as an example, removal of it not only needs etching with a special solution of hydrogen fluoride (HF) and multiple repurifying, but also may introduces ionic impurity if rinse incompletely. Therefore, it is expected that the present technique will open up a promising strategy to develop 3D structured nanotubular metal oxides, as well as perovskite oxides, with different sizes, based on adjusting the size of the PPy template.

When employed as cathode in the Li-O_2 battery, the as-prepared Co_3O_4 HPNT exhibited relatively low charge overpotential of 99 mV and high discharge/charge capacity of

4164/4299 mAh g^{-1}. This promising performance is ascribed to the 3D web-like nanoporous tubular structure, which provides rapid oxygen flow, increases the catalytic utilization of Co_3O_4, offers sufficient volume for insoluble Li_2O_2 deposition. Meanwhile, the hierarchical porous structure, including meso/nanopores on the walls of the nanotubes, facilitates O_2 diffusion, wetting by the electrolyte, and mass transport of all the reactants.

2. Results and Discussion

2.1 Structure and Morphology Analysis

Figure 1 illustrates the preparation process for the 3D Co_3O_4 HPNT. Firstly, PPy nanofibers were prepared via a polymerization method. Next, Co_3O_4/PPy precursor was achieved by a hydrothermal reaction at 150 °C for 3 h[34, 35], in which PPy nanofibers were uniformly dispersed in a mixed solvent of distilled water and ethanol with cobalt (II) acetate dissolved. Finally, the Co_3O_4/PPy precursor was heated at 450 °C for 6 h in air atmosphere to obtain the 3D hierarchical porous Co_3O_4 nanotube (Co_3O_4 HPNT) network.

A scanning electron microscope (SEM) image of PPy is shown in Figure 2a. It can be clearly observed that PPy features a homogeneous cross-linked nanofibrous web structure, with the diameters of the nanofibers in the range of 80-90 nm. After the hydrothermal reaction, the Co_3O_4 coating on the PPy nanofibers in Figure 2b keeps the nanofibrous web structure, except that the surfaces of the fibers become rough and are decorated with a uniform layer of Co_3O_4 nanoparticles. Such small Co_3O_4 particles are attributed to NH_3 coordination with cobalt cations, which tends to reduce particle size [23, 36] . The low magnification SEM image of the as-prepared Co_3O_4 HPNT in Figure 2c shows a 3D cross-linked net structure consisting of homogeneous nanotubes approximately 100 nm in diameter. The high magnification SEM image in Figure 2d shows numerous pores between the small Co_3O_4 nanocrystals on the walls of the tubes. The transmission electron microscope (TEM) image in Figure 2e shows the apparent tubular structure of the as-prepared Co_3O_4, in which the wall thickness of the tube is

about 10 nm. Furthermore, obvious mesopores about 4 nm in size on the nanowalls can be clearly observed from Figure 2f, which might be due to outward diffusion of decomposed gases from the PPy during the heating process [37]. Note that the particle size (~10 nm) of the Co_3O_4 HPNT is slightly larger than that in the Co_3O_4/PPy composite, which may be due to the crystal growth during the heat treatment [38]. An SEM image of Co_3O_4 nanoparticles (Co_3O_4 NP) prepared without the PPy nanofiber template as a control sample is shown in Figure S1 in the Spporting Information, in which serious agglomeration of nanoparticles can be clearly seen. From the high-resolution TEM (HRTEM) image in Figure 2g, it can be observed that the nanotube consists of several Co_3O_4 nanoparticles connected tightly to each other with the typical interplanar spacings of 0.28, 0.24, and 0.2 nm, consistent with the *d*-spacing of the (220), (311), and (400) crystal planes of spinel phase Co_3O_4, respectively[39]. The indexed diffraction rings in the selected area electron diffraction (SAED) pattern in Figure 2h also confirmed the spinel phase of Co_3O_4[40]. The X-ray diffraction (XRD) patterns of the Co_3O_4 HPNT and the Co_3O_4/PPy precursor are shown in Figure 2i, from which several typical diffraction peaks of the (220), (311), (400), (511), and (440) planes, assigned to spinel Co_3O_4 (JCPDS 43-1003), can be observed for both the Co_3O_4 HPNT and the Co_3O_4/PPy precursor[35, 41].

The N_2 adsorption-desorption isotherms and the pore-size distribution of the as-prepared Co_3O_4 HPNT are shown in Figure S2 in the Supporting Information. The nitrogen sorption curves exhibit the combined characteristics of type II/IV, according to the International Union of Pure and Applied Chemistry (IUPAC) classification[42], with a specific surface area of 38.1 $m^2\ g^{-1}$ and a total pore volume of 0.43 $cm^3\ g^{-1}$. The H1 hysteresis loop in the relative pressure (P/P^0) range of 0.6-1.0 is indicative of mesoporosity[43]. The pores in size of 3.8 nm attribute to the interspace voids between the Co_3O_4 nanoparticles on the tube, which is well consistent with the TEM results in Figure 2f. The pores 96 nm in size correspond to the

internal diameter of the Co_3O_4 nanotubes due to the pyrolysis of the PPy nanofibers. The specific surface area of the Co_3O_4 NPs was measured to be 29.8 m^2 g^{-1}, much lower than that of the Co_3O_4 HPNT network. To determine the calcination temperature for obtaining the Co_3O_4 HPNT from the Co_3O_4/PPy precursor, thermogravimetric (TGA) measurements in air atmosphere of the Co_3O_4/PPy precursor were performed, as shown in Figure S3. Since all the mass loss attributed to PPy burning took place below 450 °C, 450 °C was then chosen for heating the Co_3O_4/PPy precursor, and the thus-obtained Co_3O_4 HPNT shows no mass loss in the TGA plot, indicating that no PPy remains in the target Co_3O_4 HPNT network product.

2.2 Electrochemical performances on RDE

To investigate the electrocatalytic activities of the as-prepared Co_3O_4 HPNT and Co_3O_4 NP, electrochemical measurements were carried out on a rotating disk electrode (RDE) in 0.1 M KOH solution at a scan rate of 10 mV s^{-1}. Standard commercial Pt/C (20 wt% Pt on Vulcan XC-72 carbon) was also tested for comparison. Linear sweep voltammetry (LSV) curves at various rotation speeds in the potential range of -0.9 - 0.1 V (*vs.* AgCl/Ag) in O_2-saturated atmosphere were collected to determine the samples' ORR kinetic performance, which is shown in Figure S4a-4c (Supporting Information). As shown in the LSV curves in **Figure 3**a, compared with the Co_3O_4 NP, the Co_3O_4 HPNT network shows a slightly more positive onset potential and a higher reduction current density, indicating its higher ORR activity[26]. Figure S4d shows that the electron transfer number of the Co_3O_4 HPNT reached 3.5, it's much higher than that of the Co_3O_4 NP with 2.6, but a bit lower than commercial 20% Pt/C, which offers a $4e^-$ oxygen reduction reaction, suggesting that the Co_3O_4 HPNT delivers a more efficient electron transfer process[44]. The Tafel plots of the measured potential *vs.* specific ORR activity in Figure 3b, obtained from Figure 3a, indicate that the ORR activity of the Co_3O_4 HPNT network is definitely superior in terms of a smaller Tafel slope (~ 175 mV per decade) than that of the Co_3O_4 NP (~ 230 mV per decade).[23, 24] We also extended the

potential to 0.9 V (*vs.* AgCl/Ag) to the water oxidation regime and evaluated the electrocatalytic oxygen evolution reaction (OER) activities of all the above samples. The electrocatalytic OER plots in Figure 3c demonstrates that the Co_3O_4 HPNT network offers a higher current density than commercial Pt/C, with a value of more than 12 mA cm^{-2} and an onset potential of 0.7 V *vs.* AgCl/Ag, suggesting strong OER activity of the Co_3O_4 HPNT network in the aqueous system[24, 26, 34]. The above electrochemical evaluations prove that the Co_3O_4 HPNT network possesses powerful bifunctional electrocatalytic activities towards both the oxygen reduction reaction and the oxygen evolution reaction. This is because the fundamental features of the ORR and OER processes in aqueous and non-aqueous electrolytes share similarities [45-47], which will provide some enlightenment for developing efficient catalysts when shifting Li-O_2 batteries from aqueous to non-aqueous systems [24, 26]. To certify this, the as-prepared Co_3O_4 HPNT network, Co_3O_4 NP, and Ketjen Black (KB) catalyst were then subjected to steady-state cyclic voltammetry (CV) within a potential window of 2.35 - 4.35 V (*vs.* Li^+/Li) in O_2-saturated 0.2 M $LiCF_3SO_3$ in tetrathylene glycol dimethyl ether (TEGDME) with a scan rate of 10 mV s^{-1} (Figure 3d). Compared with the Co_3O_4 NP and KB, the as-prepared Co_3O_4 HPNT network exhibits obviously more apparent ORR and OER peaks in the O_2-saturated non-aqueous electrolyte, which indicates that the Co_3O_4 HPNT network features bifunctional catalyst performance in the anodic and cathodic scan processes.

2.3 Electrochemical performance in Li-O_2 batteries

The electrochemical properties of the as prepared Co_3O_4 HPNT network were studied in a coin-type lithium-oxygen cell using O_2-saturated 1.0 M $LiCF_3SO_3$ in TEGDME. Co_3O_4 NP and Ketjen Black (KB) were also investigated as controls. All the capacities reported in this work are normalized by the mass of active material and the carbon used in the cathodes.

Figure 4a presents the initial galvanostatic discharge/charge curves of a lithium oxygen battery with a Co_3O_4 HPNT network cathode and those of Co_3O_4 NP and KB cathodes at a current density of 25 μA cm^{-2} from 2.35 to 4.35 V (*vs.* Li^+/Li). Clearly, the lithium oxygen battery with the as-prepared Co_3O_4 HPNT network cathode yields the largest discharge/charge capacity of 4299/4164 mAh g^{-1} compared with the other two cathodes, and in particular, there is a much reduced charge overpotential of 99 mV from 125 mV for the Co_3O_4 NP and 111 mV for the KB cathode, showing that the as-prepared Co_3O_4 HPNT network cathode has the highest reversible discharge/charge characteristics compared to the Co_3O_4 NP and KB cathodes. Figure 4b presents the initial discharge/charge curves of the Co_3O_4 HPNT network, Co_3O_4 NP, and KB cathodes with a fixed capacity of 1000 mAh g^{-1} at a current density of 25 μA cm^{-2}, from which the lowest discharge/charge overpotential can also be observed for the Co_3O_4 HPNT network cathode. The typical selected discharge/charge profiles of the as prepared Co_3O_4 HPNT, Co_3O_4 NP, and KB cathodes with a fixed capacity of 1000 mAh g^{-1} at a current density of 25 μA cm^{-2} are presented in Figure 4c, 4d, and 4e, respectively, from which a lower discharge/charge overpotential at each cycle and rather stable discharge/charge profiles were achieved for the Co_3O_4 HPNT network cathode. Figure 4f exhibits the terminal discharge voltages for each cycle of the above three cathodes at a fixed discharge/recharge capacity of 1000 mAh g^{-1}. The discharge/charge profiles from the 1^{st} to the 20^{th} cycle for the Co_3O_4 HPNT network cathode almost overlap (Figure 4c), and the specific capacity suffers no loss, with terminal discharge/charge voltages of 2.71/4.11 V after 20 cycles and 2.22/4.56 V after 40 cycles, respectively. The terminal discharge voltage becomes lower than 2 V after 28 cycles, however, for the Co_3O_4 NP cathode and 15 cycles for the KB cathode with such a capacity limitation. From the comparison of the above results for the as-prepared Co_3O_4 HPNT network, Co_3O_4 NP, and KB cathodes, it is believed that the as-prepared 3D hierarchical porous nanotube network with Co_3O_4 nanocrystals connected to

each other on the tube surface can create a substantial amount of tri-phase and reaction sites for the Li_2O_2 formation and meanwhile provide sufficient deposition space for Li_2O_2. In addition, Co_3O_4 can take full advantage of its intrinsic catalytic activity, bringing improved ORR and OER performance [39].

2.4 Analysis of the discharge/recharge products

The XRD patterns of the as prepared Co_3O_4 HPNT network cathode in different states for the first cycle between 2.35-4.35 V (*vs*. Li^+/Li) and the recharge state after 40 cycles at a fixed capacity of 1000 mAh g^{-1} and a current density of 25 μA cm^{-2} are shown in Figure 5a. As compared with the XRD pattern of the fresh electrode, two new diffraction peaks appear in the discharged cathode, which could be reasonably assigned to the (100) and (101) peaks of crystalline Li_2O_2 (as highlighted in Figure 5a) [24, 26]. These two peaks disappear when the battery is recharged to 4.35 V, suggesting almost complete decomposition of the Li_2O_2 during the recharge process. Only peaks attributable to Co_3O_4 can be found in the XRD pattern of the as prepared Co_3O_4 HPNT network cathode after 40 fixed capacity cycles, further evidencing the highly stable catalytic activity of the as-prepared Co_3O_4 HPNT network catalyst.

The Li 1s spectra of the 1st cycle discharged, 1st cycle recharged, and 40th cycle recharged states with a fixed capacity of 1000 mAh g^{-1} for the as-prepared Co_3O_4 HPNT network cathode presented in Figure 5b are well consistent with the XRD results discussed above, where the peak at 54.6 eV can be assigned to the Li–O bond of Li_2O_2 after the 1st discharge [48-51]. Upon charging, the Li 1s peak at 54.6 eV corresponding to Li_2O_2 disappears, and no other peaks are left, showing almost complete decomposition of Li_2O_2. After the 40th cycle recharge, an obvious Li–O bond of the Li_2CO_3 signal appears in the X-ray photoelectron spectroscopy (XPS) spectrum [51]. Although TEGDME is reported to be more stable compared with other organic solvents, ether-based electrolyte decomposition still occurs [52]. According

to published reports, ether-based electrolyte is prone to auto-oxidation under oxygenated radicals, and decomposition occurs at voltages higher than 4 V, leading to the formation and accumulation of non-reversible reaction products [52, 53].

The Co_3O_4 HPNT network cathode was monitored during the discharging and charging processes at a current density of 25 μA cm^{-2}, using ex-situ scanning electron microscopy (SEM), as presented in Figure 6b-f, corresponding to the states (b-f) in Figure 6a. The fresh Co_3O_4 HPNT network cathode in Figure 6b reveals a porous morphology because of the web-like Co_3O_4 nanotubes with KB particles aggregated on the surfaces of the nanotubes. When the Co_3O_4 HPNT network cathode is discharged to 1500 mAh g^{-1}, a small amount of film consisting of the discharge product Li_2O_2 grown on the cathode surface can be observed in Figure 6c. When the discharge voltage goes down to 2.35 V, there is a large amount of porous Li_2O_2 discharge product, consisting of many nanofilms that completely cover the cathode. It is noteworthy that the Li_2O_2 discharge product formed on the Co_3O_4 HPNT network catalytic cathode is in sharp contrast to the conventional toroidal [49, 54-56] or plate [57] morphology of the Li_2O_2 discharge product. Nazar *et al.* [56] found that large toroidal-shaped crystalline Li_2O_2 tends to form at low current densities, while higher current densities favor film formation of Li_2O_2. Zhang *et al.* [48], however, reported that the film-like Li_2O_2 with low crystallinity may contain many defects (for example, lithium vacancies) that facilitate electron transportation and especially ion conduction, thus reducing the charge overpotential [58, 59], which further explains the much reduced charge overpotential of the as-prepared Co_3O_4 HPNT network cathode. When the Li-O_2 battery with the Co_3O_4 HPNT network cathode was recharged to the capacity of 3000 mAh g^{-1}, only a little film-like Li_2O_2 was left, as shown in Figure 6e. All the discharge products disappear when the Li-O_2 battery is fully charged to 4.35 V. Also, the porous and 3D web-like nature of the Co_3O_4 HPNT network cathode is regained (Figure 6f), similar to the fresh one in Figure 6b, indicating the reversible reaction

of Li_2O_2. Figure 6g provides the schematic illustration of the Co_3O_4 electrode, in which carbon particles (Ketjen Black) dispersed in Co_3O_4 nanoweb ensuring rapid charge transfer. Macropores between Co_3O_4 nanotubes facilitate high O_2 transportation whereas nano-and meso-pores in the Co_3O_4 HPNT provide quantities of catalytic active sites and benefit electrolyte wetting. Combined with sufficient triple-phase sites, porous like Li_2O_2 consisting nano films grow uniformly on the surface of the cathode after discharge and disappear after charge. Since Li-O_2 batteries are still in their infancy stage, further research efforts, including in-situ TEM observations, should be devoted to clarifying the effects of the morphology of Li_2O_2 on the discharge/charge process of Li-O_2 batteries.

Electrochemical impedance spectroscopy (EIS) tests of the as-prepared Co_3O_4 HPNT network cathode at different discharge/recharge stages were performed to further identify the discharge and recharge characteristics, as is shown in Figure S5. A larger charge-transfer resistance is observed after the first discharge compared with the fresh electrode due to the formation of Li_2O_2, which has high electrical resistivity and is hypothesized to prevent the transfer of electrons[60]. After the battery was recharged, however, the charge-transfer resistance of the Co_3O_4 HPNT network electrode was little changed compared with the fresh state, suggesting reversible reaction product formation and decomposition. The charge-transfer resistance increases again after the 40^{th} recharge due to the formation and accumulation of non-reversible reaction products[52, 53], which is well consistent with the results of XRD and the field emission SEM image in Figure 5 and Figure 6, respectively. This provides electrochemical evidence that the as-prepared Co_3O_4 HPNT network can effectively catalyze both the ORR and OER reactions in rechargeable lithium-oxygen batteries.

3. Conclusion

In summary, this work describes a facile and large-scale approach to the fabrication of a 3D hierarchical porous Co_3O_4 nanotube (HPNT) network by using polypyrrole nanofiber as the sacrificial template. The as-prepared 3D Co_3O_4 HPNT network demonstrated superior bifunctional electrocatalytic activity towards both the ORR and the OER when employed as the catalyst in non-aqueous lithium oxygen batteries, as compared to Co_3O_4 nanoparticles (Co_3O_4 NP) and Ketjen Black (KB) catalysts. The Li-O_2 battery based on Co_3O_4 HPNT network cathode shows a relative low charge overpotential of 99 mV and high discharge/charge capacity of 4164/4299 mAh g^{-1}, as well as a long lifespan of 40 cycles at a fixed capacity of 1000 mA g^{-1}. These encouraging results may provide insights into the use of polymer nanofiber as new template to develop 3D porous tubular structured catalyst for Li-O_2 batteries on a large scale and in a rapid way.

4. Experimental section

4.1 Material preparation

4.1.1 Preparation of PPy nanofibers

PPy nanofibers were synthesized via an oxidative template assembly route. Pyrrole (Py) was distilled before use. In a typical process, 0.72 g cetrimonium bromide (CTAB) was dissolved in 200 mL of 1 M HCl solution by constant stirring in an ice bath (0-5 ºC). Subsequently, 0.33 g distilled Py monomer was added into the above solution, and another 0.5 h stirring was carried out. Meanwhile, 1.13 g ammonium persulfate (APS) was dissolved in 20 mL distilled water which was then dropped into the Py monomer-containing solution and allowed to react for 24 h in an ice bath (0-5 ºC). After that, the black product was suction filtered and washed several times with 1 M HCl solution and distilled water, followed by drying in a vacuum oven at 80 ºC overnight. Finally, a black powder was yielded and denoted as PPy nanofiber.

4.1.2 Preparation of Co_3O_4 nanotube (HPNT) network

In a typical synthesis [34, 35], 0.4125 g cobalt (II) acetate was dissolved in 15 mL distilled water and 26 mL ethanol mixed solvent. Then, 50 mg of PPy nanofibers was added into the mixed solution, which was ultrasonically treated for 1 h. Secondly, 1.5 ml 25% ammonium was added under vigorous stirring. The mixture was stirred in air for about 10 min to form a homogeneous dark slurry. Then, the suspension was transferred into a 120 mL autoclave, sealed, and maintained at 150 ºC for 3 h. Afterwards, the autoclave was cooled to room temperature naturally. The resulting black solid products were washed with water via centrifugation and re-dispersion and dried in a vacuum oven at 80 ºC overnight, which was followed by a heat-treatment at 450 ºC for 6 h in air atmosphere. Meanwhile, pristine Co_3O_4 under the same hydrothermal conditions without PPy nanofiber as template was also prepared as a control sample, with the sample denoted as Co_3O_4 NP.

4.2 Physical characterizations

X-ray diffraction (XRD) (GBC MMA) patterns were collected over a 2θ range of 20º- 70º with a scan rate of 4 º min^{-1} and analysed with Traces™ software in combination with the Joint Committee on Powder Diffraction Standards (JCPDS) powder diffraction files. The morphologies of the samples were examined by field emission scanning electron microscopy (FE-SEM, JEOL 7500) and transmission electron microscopy (TEM, JEOL ARM-200F). The XPS data were analysed using CasaXPS software, and all the results were calibrated by C 1s at 284.6 eV for graphite. Thermogravimetric analysis (TGA) was carried out using a SETARAM Thermogravimetric Analyzer (France). Brunauer-Emmett-Teller (BET) surface area and pore size distribution (PSD) measurements were conducted by N_2 adsorption/desorption at 77 K on a Quantachrome Autosorb-IQ MP instrument.

4.3 Li-O_2 battery measurements

The electrochemical performance of lithium-oxygen batteries containing the samples as active materials was investigated using 2032 coin-type cells with air holes on the cathode side.

For the preparation of the porous cathode electrode, 60 wt.% catalyst, 30 wt.% Ketjen Black (KB), and 10 wt.% poly(1,1,2,2-tetrafluoroethylene) (PTFE) (60% dispersion) were mixed in an isopropanol solution. The resulting homogeneous slurry was coated on carbon paper. The same procedure was applied to prepare pristine KB electrodes. After that, the electrodes were dried at 120 ºC in a vacuum oven for 12 h. All the lithium-oxygen batteries were assembled in an Ar-filled glove box (Mbraun, Unilab, Germany) with both water and oxygen contents below 0.1 ppm. They consisted of lithium metal foil as the counter electrode, a glass fiber separator (Whatman GF/D), non-carbonate electrolyte containing 1 M $LiCF_3SO_3$ dissolved in tetraethylene glycol dimethyl ether (TEGDME), and the air cathode electrode. All the assembled coin cells were stored in an O_2-purged chamber which was connected to a LAND CT 2001 instrument, a multi-channel battery tester, for 2 h before each test. The galvanostatic discharge-charge tests were then conducted on the battery testing system with the voltage between 2.35-4.35 V (*vs*. Li^+/Li), and the capacities reported in this work were normalized by the mass of active material and carbon used in the cathodes. The loading amount in each cathode was approximately 1 mg cm^{-2}. Cyclic voltammetry (CV) was conducted in O_2-saturated 0.2 M lithium trifluoromethanesulfonate ($LiCF_3SO_3$) in tetraethylene glycol dimethyl ether (TEGDME) with a scan rate of 10 mV s^{-1}.

Examination of the discharged and recharged electrodes involved disassembling the cell in the glove box, rinsing the cathode with tetraethylene glycol dimethyl ether, and removing the solvent under vacuum. For ex-situ XRD, SEM, and XPS tests, the electrodes were covered by a layer of Kapton film before moving them from the glove box to the outside instruments.

4.4 Rotating disk electrode tests

Rotating disk electrode (RDE) tests were performed using a computer-controlled potentiostat (Princeton 2273 and 616, Princeton Applied Research) in a conventional three-electrode cell at room temperature. The glassy carbon (GC) working electrode (0.196 cm^{-1}) was first

polished with alumina powder, rinsed with deionized water, and sonicated, first in ethanol and then in double-distilled water. A platinum wire and Ag/AgCl (filled with saturated KCl aqueous solution) were used as the counter and reference electrodes, respectively. Typically, the catalyst was redispersed in deionized water + isopropanol + 5% Nafion® (v/v/v = 4/1/0.05) to form a homogeneous catalyst ink with a concentration of 2 mg mL^{-1}. Then, 30 μL of this dispersion was pipetted onto the surface of the GC working electrode and dried under ambient conditions. For comparison, commercial Pt/C (20 wt. % Pt on Vulcan XC-72) catalyst ink was also obtained by the same method described above. Linear sweep voltammograms (LSVs) to measure the ORR performance were collected in O_2 saturated 0.1 M KOH solution with different rotation speeds from 400 to 1600 rpm from -0.9 − 0.1 V with a scan rate of 10 mV s^{-1}, while OER plots were obtained in Ar atmosphere from 0.1 − 0.9 V with a scan rate of 10 mV s^{-1} and a rotation speed of 1600 rpm.

Koutecky-Levich (K-L) plots show the inverse current density (j^{-1}) as a function of the inverse of the square root of the rotation speed ($\omega^{-1/2}$) at different potentials. The number of electrons involved per O_2 in the ORR was determined by the Koutecky-Levich equation:[8a, 28]

$$\frac{1}{j} = \frac{1}{j_k} + \frac{1}{j_d} = \frac{1}{B\omega^{1/2}} + \frac{1}{j_k} \qquad (1)$$

where j, j_k, and j_d are the measured, the kinetically controlled, and the diffusion controlled current densities, respectively, and ω is the electrode rotation rate. B is determined from the slope of the K-L plot based on the Levich equation:

$$B = 0.2nF(D_{O_2})^{2/3} v^{-1/6} C_{O_2} \qquad (2)$$

where n represents the number of electrons gained per O_2, F is the Faraday constant (F = 96485 C mol^{-1}), D_{O_2} is the diffusion coefficient of O_2 in 0.1 M KOH (1.9×10^{-5} cm^2 s^{-1}), v is the kinetic viscosity (0.01 cm^2 s^{-1}), and C_{O_2} is the bulk concentration of O_2 (1.2×10^{-6} mol cm^{-3}).

Supporting Information

Supporting Information is available from the Wiley Online Library or from the author.

Acknowledgements

Financial support from an Australian Research Council (ARC) Discovery Project (DP140100401) and the Distinguished Young Scientists Program of the National Natural Science Foundation of China (No. 51425301) is greatly appreciated. The authors also are grateful for the use of the facilities in the UOW Electron Microscopy Center. Many thanks also go to Dr. Tania Silver for critical reading of the manuscript. The authors would like to thank the Australian National Fabrication Facility (ANFF) for equipment access.

Received: ((will be filled in by the editorial staff))

Revised: ((will be filled in by the editorial staff))

Published online: ((will be filled in by the editorial staff))

1. C. Liu, E. I. Gillette, X. Chen, A. J. Pearse, A. C. Kozen, M. A. Schroeder, K. E. Gregorczyk, S. B. Lee and G. W. Rubloff, *Nat Nanotechnol*, 2014, **9**, 1031-1039.
2. F. Wang, X. Wu, C. Li, Y. Zhu, L. Fu, Y. Wu and X. Liu, *Energy Environ. Sci.*, 2016, DOI: 10.1039/c6ee02070d.
3. S. J. C. Sang Hoon Joo, Ilwhan Oh, Juhyoun Kwak, Zheng Liu, Osamu Terasaki, Ryong Ryoo, *Nature*, 2001, **412**, 169-173.
4. P. B. Antonino Salvatore Arico, Bruno Scrosati, Jeanmarie Tarascon, Walter Van Schalkwijk, *Nature*, 2005, **4**, 366-377.
5. L. S. Zhong, J. S. Hu, H. P. Liang, A. M. Cao, W. G. Song and L. J. Wan, *Advanced materials*, 2006, **18**, 2426-2431.
6. Z. Guo, D. Zhou, X. Dong, Z. Qiu, Y. Wang and Y. Xia, *Advanced materials*, 2013, **25**, 5668-5672.
7. Q. Zhang, E. Uchaker, S. L. Candelaria and G. Cao, *Chemical Society reviews*, 2013, **42**, 3127-3171.
8. B. C. Steele and A. Heinzel, *Nature*, 2001, **414**, 345-352.
9. J. Wang, Y. Li and X. Sun, *Nano Energy*, 2013, **2**, 443-467.
10. K. T. Nam, D.-W. Kim, P. J. Yoo, C.-Y. Chiang, N. Meethong, P. T. Hammond, Y.-M. Chiang and A. M. Belcher, *Science*, 2006, **312**, 885-888.
11. C. K. Chan, H. Peng, G. Liu, K. McIlwrath, X. F. Zhang, R. A. Huggins and Y. Cui, *Nature nanotechnology*, 2008, **3**, 31-35.
12. Y. Shi, S.-L. Chou, J.-Z. Wang, D. Wexler, H.-J. Li, H.-K. Liu and Y. Wu, *Journal of Materials Chemistry*, 2012, **22**, 16465-16470.
13. F. Wang, C. Wang, Y. Zhao, Z. Liu, Z. Chang, L. Fu, Y. Zhu, Y. Wu and D. Zhao, *Small*, 2016.

14. L. Liu, Y. Hou, X. Wu, S. Xiao, Z. Chang, Y. Yang and Y. Wu, *Chemical communications*, 2013, **49**, 11515-11517.
15. Q. Qu, L. Fu, X. Zhan, D. Samuelis, J. Maier, L. Li, S. Tian, Z. Li and Y. Wu, *Energy & Environmental Science*, 2011, **4**, 3985.
16. W. Tang, Y. Hou, F. Wang, L. Liu, Y. Wu and K. Zhu, *Nano letters*, 2013, **13**, 2036-2040.
17. S. A. F. Zhangquan Peng, Yuhui Chen, and P. G. Bruce, *Science*, 2012, **337**, 563-566.
18. D. Aurbach, B. D. McCloskey, L. F. Nazar and P. G. Bruce, *Nat Energy*, 2016, **1**, 16128.
19. F. Li, T. Zhang and H. Zhou, *Energy Environ Sci*, 2013, **6**, 1125.
20. Z. Zhang, J. Bao, C. He, Y. Chen, J. Wei and Z. Zhou, *Advanced Functional Materials*, 2014, **24**, 6826-6833.
21. Z. Ma, X. Yuan, L. Li, Z.-F. Ma, D. P. Wilkinson, L. Zhang and J. Zhang, *Energy Environ Sci*, 2015, **8**, 2144-2198.
22. M. Asadi, B. Kumar, C. Liu, P. Phillips, P. Yasaei, A. Behranginia, P. Zapol, R. F. Klie, L. A. Curtiss and A. Salehi-Khojin, *ACS nano*, 2016, **10**, 2167-2175.
23. Y. Shao, F. Ding, J. Xiao, J. Zhang, W. Xu, S. Park, J.-G. Zhang, Y. Wang and J. Liu, *Advanced Functional Materials*, 2013, **23**, 987-1004.
24. L. L. Liu, Y. Y. Hou, J. Wang, J. Chen, Hua-Kun Liu, Y. P. Wu and J. Z. Wang, *Adv Mater Interfaces*, 2016, Accepted.
25. E. Tylianakis, G. K. Dimitrakakis, S. Melchor, J. A. Dobado and G. E. Froudakis, *Chemical communications*, 2011, **47**, 2303-2305.
26. L. Liu, J. Wang, Y. Hou, J. Chen, H. K. Liu, J. Wang and Y. Wu, *Small*, 2016, **12**, 602-611.
27. W. E. Teo, M. Kotaki, X. M. Mo and S. Ramakrishna, *Nanotechnology*, 2005, **16**, 918-924.
28. Y. Sun, Y. Ren, Y. Liu, J. Wen, J. S. Okasinski and D. J. Miller, *Nature Communications*, 2012, **3**, 971.
29. W. B. Luo, X. W. Gao, S. L. Chou, J. Z. Wang and H. K. Liu, *Advanced materials*, 2015, **27**, 6862-6869.
30. J. Heremans, C. Thrush, Z. Zhang, X. Sun, M. Dresselhaus, J. Ying and D. Morelli, *Physical Review B*, 1998, **58**, R10091.
31. N. Zhao, G. Wang, Y. Huang, B. Wang, B. Yao and Y. Wu, *Chemistry of Materials*, 2008, **20**, 2612-2614.
32. M. H. Park, K. Kim, J. Kim and J. Cho, *Advanced materials*, 2010, **22**, 415-418.
33. J. Chen, D. Wang, J. Qi, G. Li, F. Zheng, S. Li, H. Zhao and Z. Tang, *Small*, 2015, **11**, 420-425.
34. Y. Liang, H. Wang, P. Diao, W. Chang, G. Hong, Y. Li, M. Gong, L. Xie, J. Zhou and J. Wang, *Journal of the American Chemical Society*, 2012, **134**, 15849-15857.
35. Y. J. Sa, K. Kwon, J. Y. Cheon, F. Kleitz and S. H. Joo, *Journal of Materials Chemistry A*, 2013, **1**, 9992.
36. Y. Liang, Y. Li, H. Wang, J. Zhou, J. Wang, T. Regier and H. Dai, *Nature materials*, 2011, **10**, 780-786.
37. W. Tang, Y. Hou, F. Wang, L. Liu, Y. Wu and K. Zhu, *Nano letters*, 2013, **13**, 2036-2040.
38. C. Herring, *Journal of Applied Physics*, 1950, **21**, 301-303.
39. L. j. Li, S. y. Liu and A. Manthiram, *Nano Energy*, 2015, **12**, 852-860.
40. L. Liu, Y. Hou, J. Wang, J. Chen, H.-K. Liu, Y. Wu and J. Wang, *Adv Mater Interfaces*, 2016, **3**, 1600030.

41. Y. Dong, K. He, L. Yin and A. Zhang, *Nanotechnology*, 2007, **18**, 435602.
42. J. Xiao, D. Mei, X. Li, W. Xu, D. Wang, G. L. Graff, W. D. Bennett, Z. Nie, L. V. Saraf and I. A. Aksay, *Nano letters*, 2011, **11**, 5071-5078.
43. S. Ma, L. Sun, L. Cong, X. Gao, C. Yao, X. Guo, L. Tai, P. Mei, Y. Zeng and H. Xie, *The Journal of Physical Chemistry C*, 2013, **117**, 25890-25897.
44. J. Wang, L. Liu, S. Chou, H. Liu and J. Wang, *J. Mater. Chem. A*, 2016, DOI: 10.1039/c6ta07050g.
45. Z. L. Wang, D. Xu, J. J. Xu and X. B. Zhang, *Chemical Society reviews*, 2014, **43**, 7746-7786.
46. F. Cheng and J. Chen, *Chemical Society reviews*, 2012, **41**, 2172-2192.
47. H. W. Park, D. U. Lee, M. G. Park, R. Ahmed, M. H. Seo, L. F. Nazar and Z. Chen, *ChemSusChem*, 2015, **8**, 1058-1065.
48. Q. C. Liu, J. J. Xu, D. Xu and X. B. Zhang, *Nat Commun*, 2015, **6**, 7892.
49. F. Li, D. M. Tang, Z. Jian, D. Liu, D. Golberg, A. Yamada and H. Zhou, *Advanced materials*, 2014, **26**, 4659-4664.
50. Y. Chen, Q. Zhang, Z. Zhang, X. Zhou, Y. Zhong, M. Yang, Z. Xie, J. Wei and Z. Zhou, *J. Mater. Chem. A*, 2015, **3**, 17874-17879.
51. D. Kundu, R. Black, E. J. Berg and L. F. Nazar, *Energy Environ. Sci.*, 2015, **8**, 1292-1298.
52. S. A. Freunberger, Y. Chen, N. E. Drewett, L. J. Hardwick, F. Barde and P. G. Bruce, *Angewandte Chemie*, 2011, **50**, 8609-8613.
53. B. D. McCloskey, R. Scheffler, A. Speidel, D. S. Bethune, R. M. Shelby and A. C. Luntz, *Journal of the American Chemical Society*, 2011, **133**, 18038-18041.
54. J. Lu, L. Cheng, K. C. Lau, E. Tyo, X. Luo, J. Wen, D. Miller, R. S. Assary, H. H. Wang, P. Redfern, H. Wu, J. B. Park, Y. K. Sun, S. Vajda, K. Amine and L. A. Curtiss, *Nat Commun*, 2014, **5**, 4895.
55. Y.-C. Lu, B. M. Gallant, D. G. Kwabi, J. R. Harding, R. R. Mitchell, M. S. Whittingham and Y. Shao-Horn, *Energy & Environmental Science*, 2013, **6**, 750.
56. B. D. Adams, C. Radtke, R. Black, M. L. Trudeau, K. Zaghib and L. F. Nazar, *Energy & Environmental Science*, 2013, **6**, 1772.
57. R. Choi, J. Jung, G. Kim, K. Song, Y.-I. Kim, S. C. Jung, Y.-K. Han, H. Song and Y.-M. Kang, *Energy & Environmental Science*, 2014, DOI: 10.1039/c3ee43437k.
58. X. Huang, H. Yu, H. Tan, J. Zhu, W. Zhang, C. Wang, J. Zhang, Y. Wang, Y. Lv and Z. Zeng, *Advanced Functional Materials*, 2014, **24**, 6516-6523.
59. F. Tian, M. D. Radin and D. J. Siegel, *Chemistry of Materials*, 2014, **26**, 2952-2959.
60. S. Lau and L. A. Archer, *Nano letters*, 2015, **15**, 5995-6002.

Table of contents

An approach to synthesize three-dimensional (3D) hierarchical porous Co_3O_4 nanotube (HPNT) network has been proposed. Polypyrrole nanofiber (PPy NF) is used as the sacrificial template. When employed as cathode for lithium-oxygen batteries, it demonstrates superior bifunctional electrocatalytic activities towards both the oxygen reduction reaction and the oxygen evolution reaction.

3D Hierarchical Porous Co_3O_4 NanoTube Network as Efficient Cathode for Rechargeable Lithium-Oxygen Batteries

Lili Liu, Haipeng Guo, Yuyang Hou, Jun Wang, Jun Chen, Hua-Kun Liu, Jiazhao Wang and Yuping Wu**

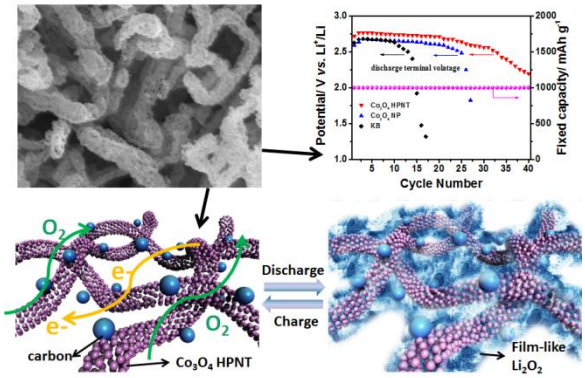

Figures and Captions

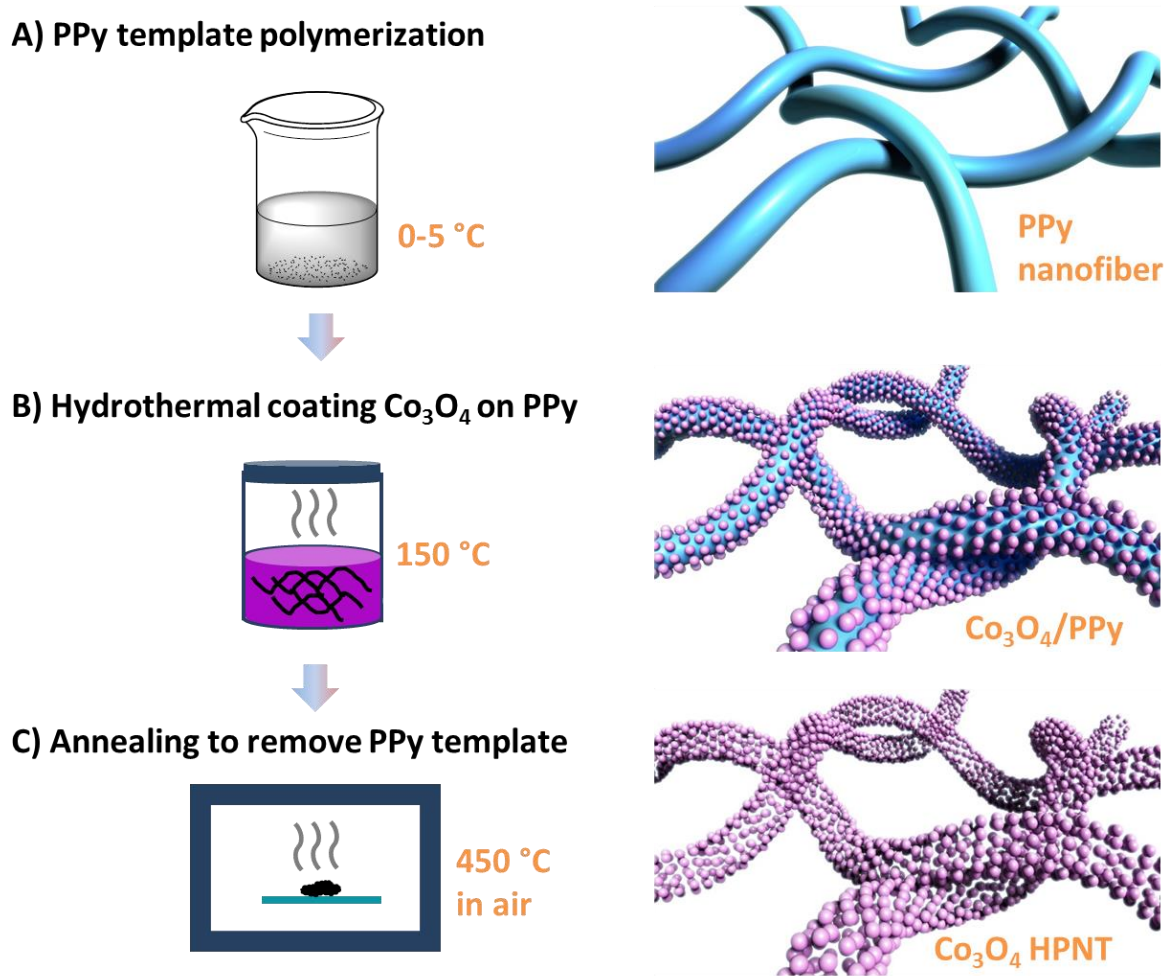

Figure 1. Schematic illustration of the fabrication of Co_3O_4 HPNT network.

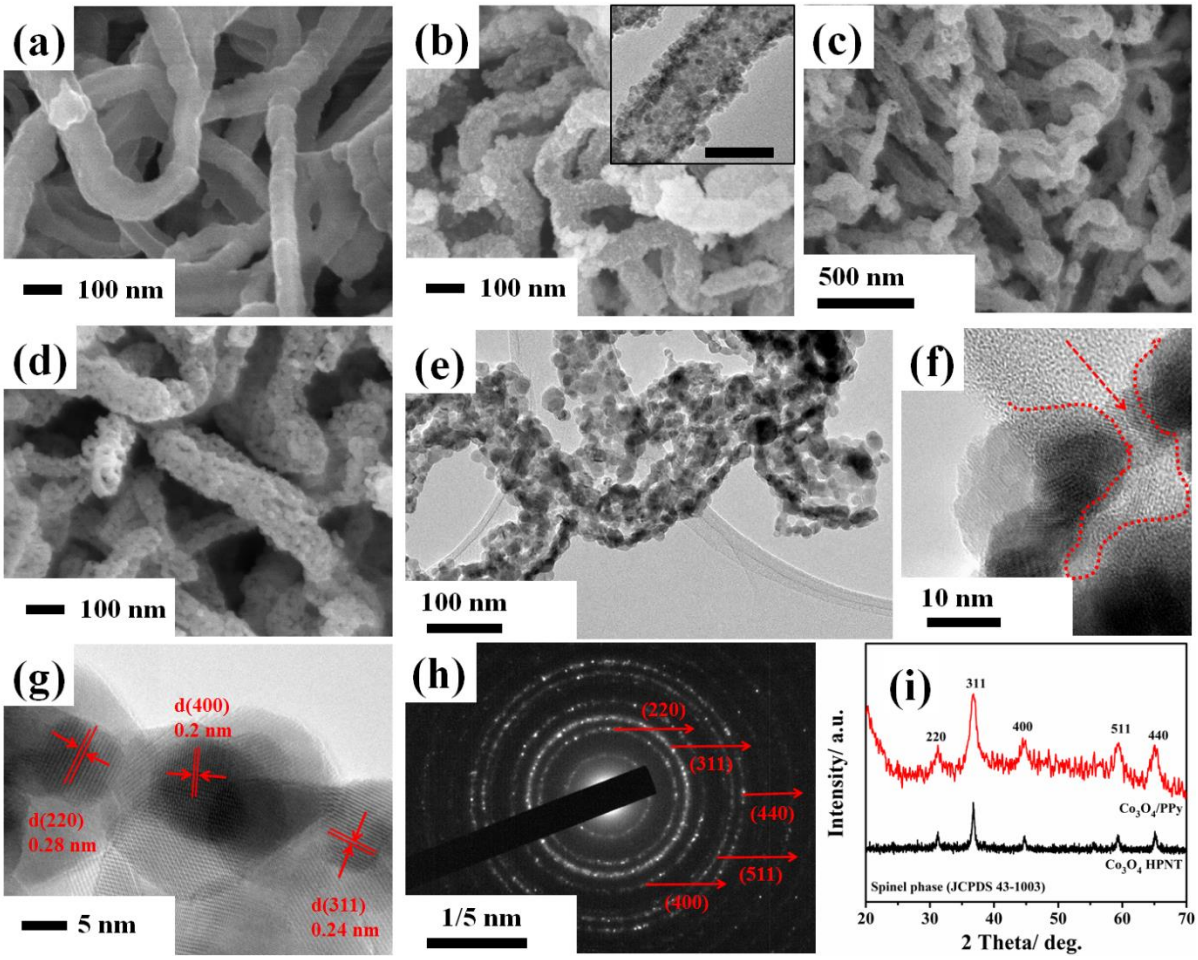

Figure 2. Physical characterization. (a) SEM image of the PPy nanofibers; (b) SEM image of the nanofibrous Co_3O_4/PPy with inset TEM image, inset bar: 100 nm; (c-d) SEM and (e-f) TEM images of Co_3O_4 HPNT network; (g) High magnification TEM image of Co_3O_4 HPNT network, (h) SAED pattern of Co_3O_4 HPNT network, and (i) XRD patterns of nanofibrous Co_3O_4/PPy and Co_3O_4 HPNT network.

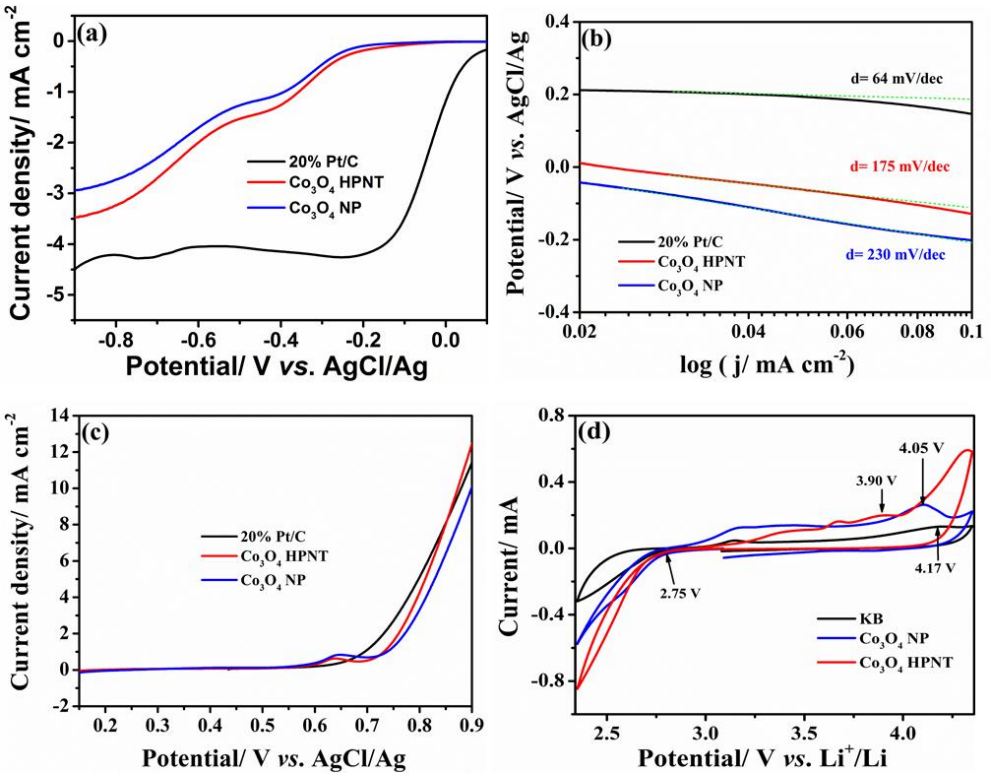

Figure 3. a) Linear sweep voltammetry (LSV) curves of commercial 20 wt.% Pt/C, the Co_3O_4 HPNT network, and Co_3O_4 NP in O_2-saturated 0.1 M KOH aqueous solution at a scan rate of 10 mV s^{-1} in the potential range of -0.9-0.1 V (*vs.* AgCl/Ag). b) Tafel plots showing the potential for commercial 20 wt.% Pt/C, the Co_3O_4 HPNT network, and Co_3O_4 NP as a function of the log of the kinetic current density, based on the data from (a). c) Oxygen evolution curves for the commercial 20 wt.% Pt/C, Co_3O_4 HPNT network, and Co_3O_4 NP in the potential range of 0.1-0.9 V (*vs.* AgCl/Ag). (d) Cyclic voltammograms of the as-prepared Co_3O_4 HPNT network, Co_3O_4 NP, and KB acquired at a scan rate of 10 mV s^{-1} in 0.2 M $LiCF_3SO_3$/TEGDME electrolyte.

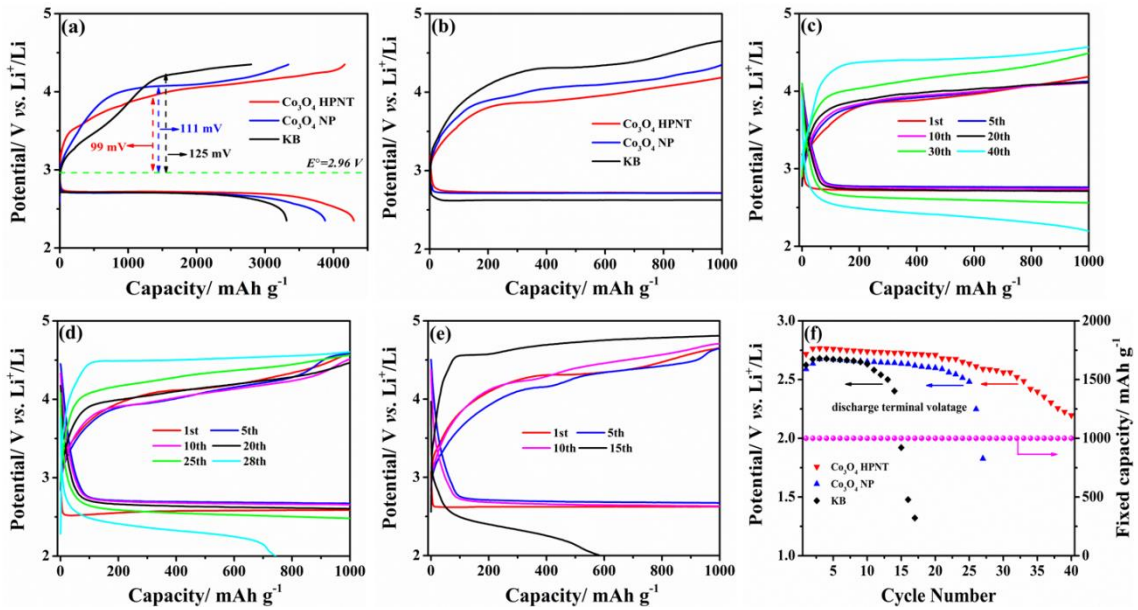

Figure 4. (a) Initial discharge-charge plots of the as-prepared Co_3O_4 HPNT network, Co_3O_4 NP, and KB cathodes in lithium-oxygen batteries at a current density of 25 μA cm^{-2} in 1 M $LiCF_3SO_3$/TEGDME, with a voltage window of 2.35-4.35 V (*vs*. Li^+/Li). (b) Initial discharge/charge plots of the Co_3O_4 HPNT network, Co_3O_4 NP, and KB cathodes in lithium-oxygen batteries at a current density of 25 μA cm^{-2} in 1 M $LiCF_3SO_3$/TEGDME with discharge/charge capacities fixed at 1000 mAh g^{-1}. Representative discharge/charge curves of (c) as-prepared Co_3O_4 HPNT network, (d) Co_3O_4 NP, and (e) KB under a capacity limit of 1000 mA h g^{-1} at a current density of 25 μA cm^{-2} in 1 M $LiCF_3SO_3$/TEGDME. (f) The corresponding terminal discharge voltage of the Co_3O_4 HPNT network, Co_3O_4 NP, and KB under a capacity limit of 1000 mA h g^{-1} at a current density of 25 μA cm^{-2} in 1 M $LiCF_3SO_3$/TEGDME.

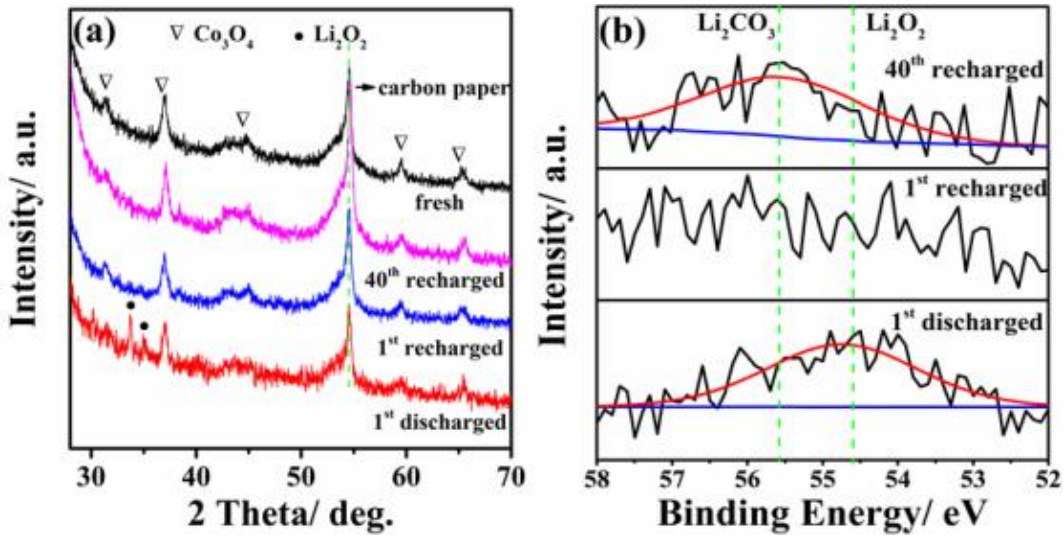

Figure 5. (a) XRD patterns of the Co_3O_4 HPNT network cathode at different discharge/charge stages, and (b) Li 1s XPS spectra of the Co_3O_4 HPNT network cathode at different discharge/charge stages.

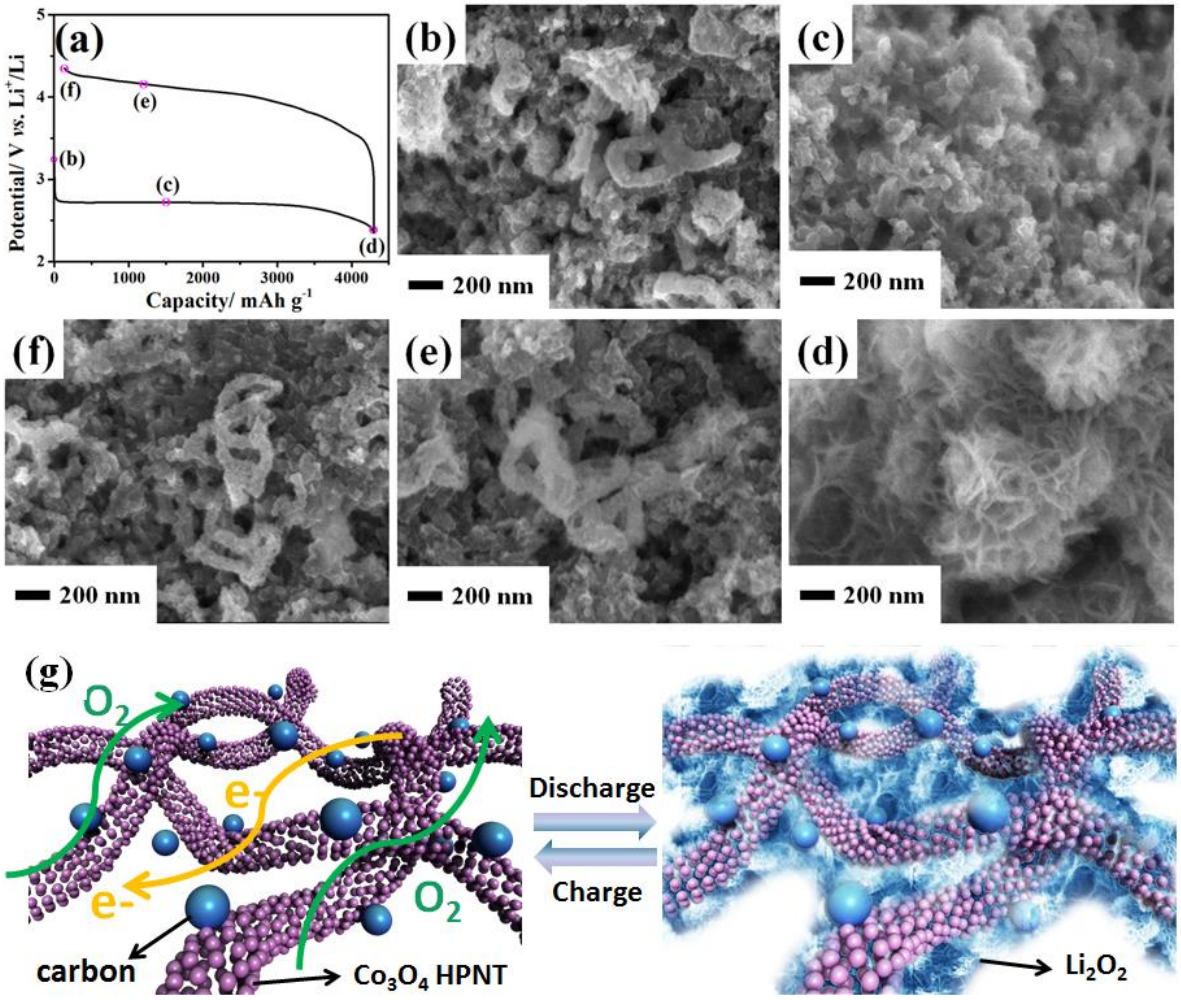

Figure 6. (a) Typical initial discharge/recharge curves of Co_3O_4 HPNT network cathode at a current density of 25 μA cm^{-2} in the voltage range of 2.35-4.35 V (*vs.* Li^+/Li) with (b), (c), (d), (e), and (f) stages. (b-f) SEM images of Co_3O_4 HPNT network cathode corresponding to (b), (c), (d), (e), and (f) stages in (a), respectively. (g) Schematic illustration of the Co_3O_4 HPNT cathode in the Li-O_2 battery system.

Supporting Information

Lili Liu, Yuyang Hou, Haipeng Guo, Weiwei Fang, Jun Wang, Jun Chen, Hua-Kun Liu, Jiazhao Wang and Yuping Wu**

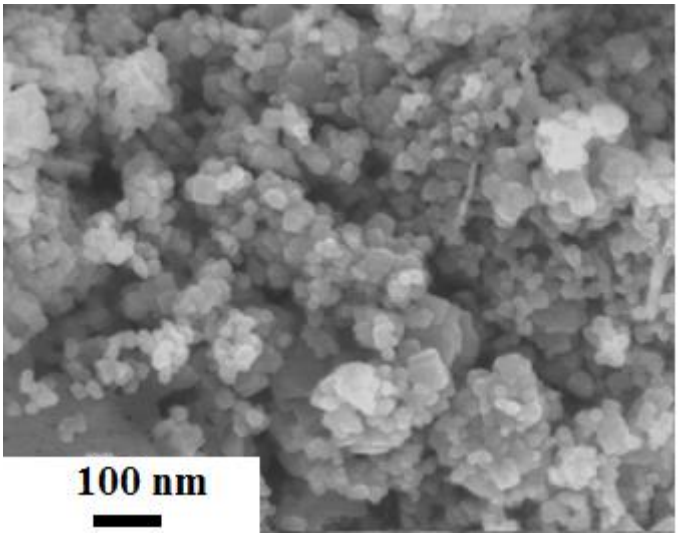

Figure S1. SEM image of Co_3O_4 nanoparticles (Co_3O_4 NP).

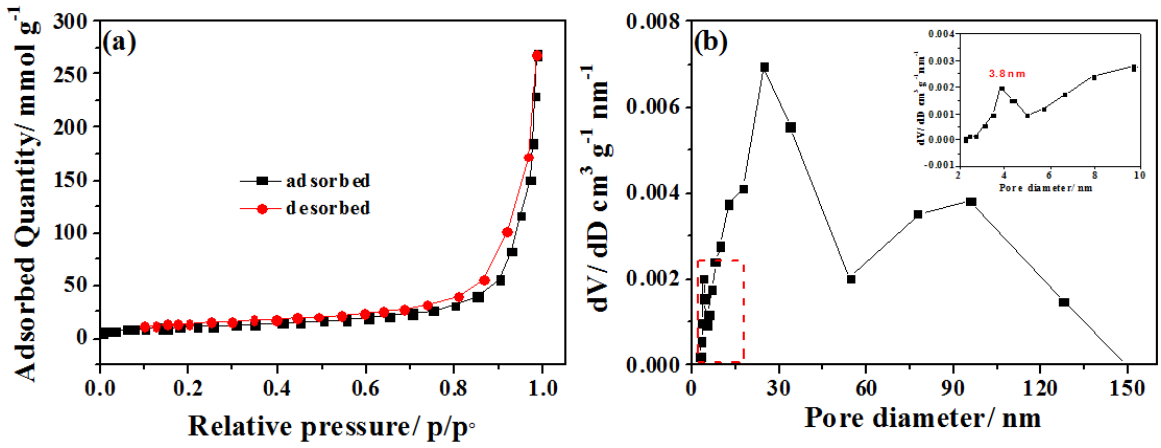

Figure S2. a) N_2 adsorption-desorption isotherms and b) pore size distribution of the as-prepared Co_3O_4 HPNT network, with the inset showing an enlargement of the indicated range.

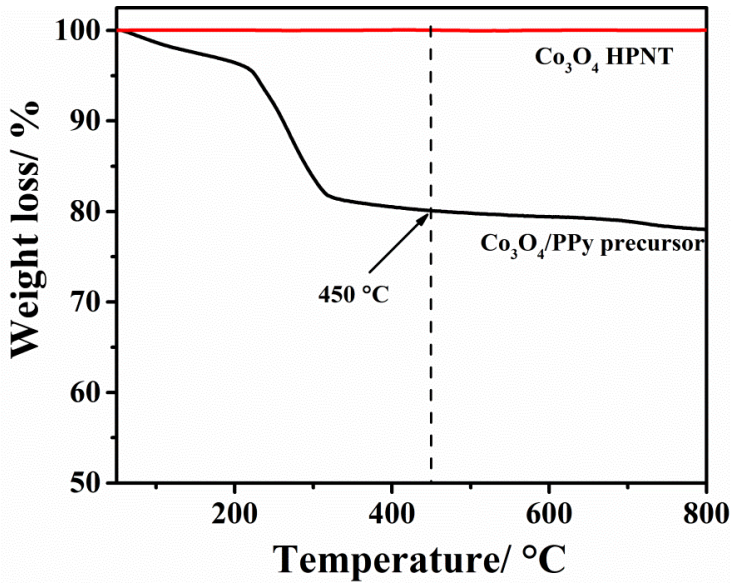

Figure S3. TGA plots of the Co_3O_4/PPy precursor and the as-prepared Co_3O_4 HPNT network.

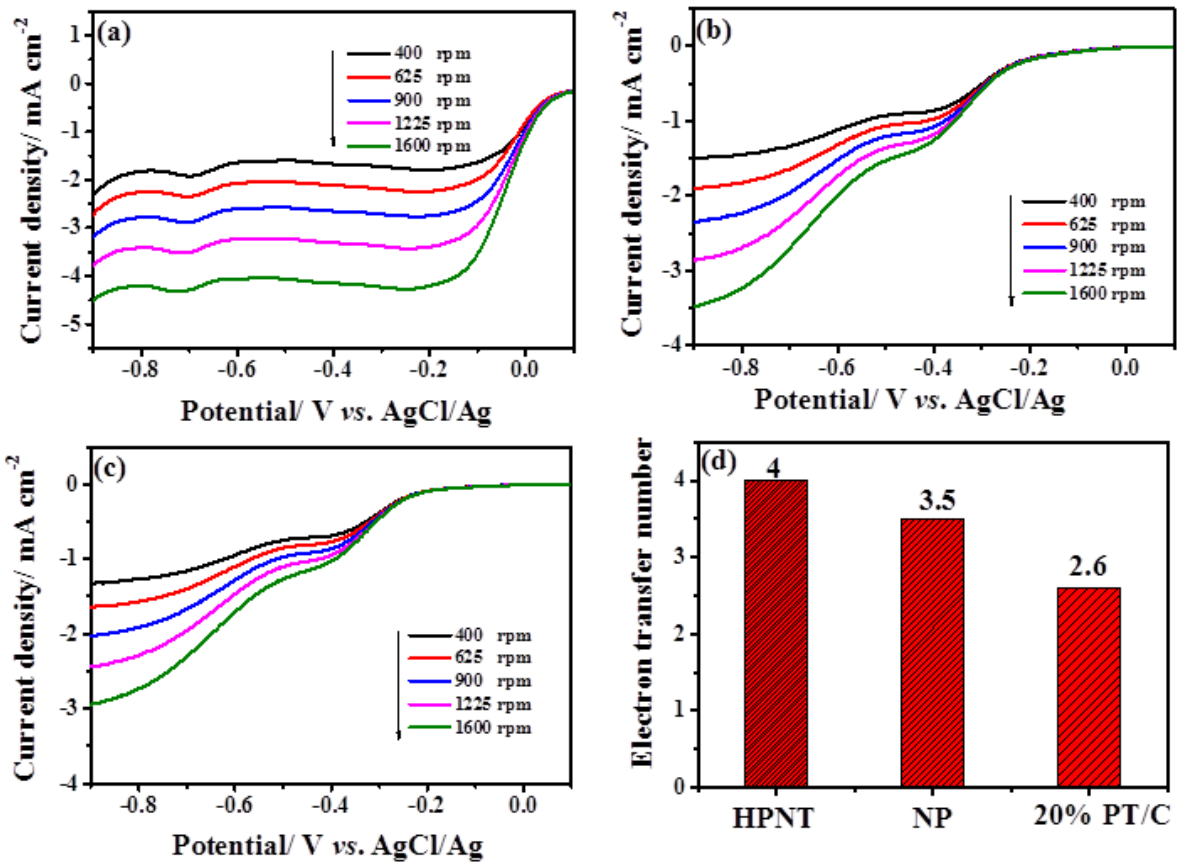

Figure S4. Linear sweep voltammetry (LSV) curves at various rotation speeds in O_2-saturated 0.1 M KOH aqueous solution at a scan rate of 10 mV s^{-1} in the potential range of -0.9-0.1 V (*vs.* AgCl/Ag) for (a) commercial 20 wt.% Pt/C, (b) the Co_3O_4 HPNT network, and (c) Co_3O_4 NP. (d) Calculated electron transfer numbers of the Co_3O_4 HPNT, Co_3O_4 NP and 20% Pt/C from the LSV curves.

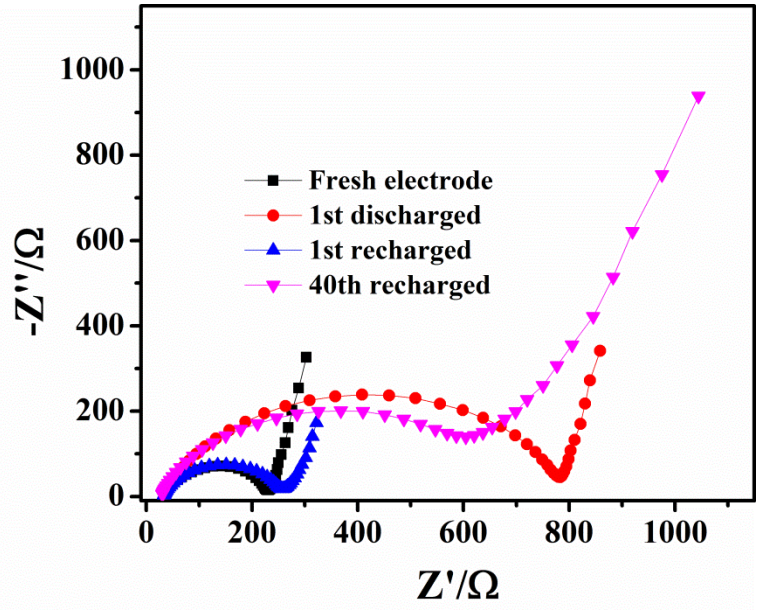

Figure S5. Electrochemical impedance spectroscopy (EIS) plots of the as-prepared Co_3O_4 HPNT network in fresh, 1st cycle discharged, 1st cycle recharged, and 40th cycle recharged states.